Proceedings of ASME 2024 Conference on Smart Materials,
Adaptive Structures and Intelligent Systems
SMASIS2024
September 9-12, 2024, Atlanta, Georgia

Draft-SMASIS2024-140049

HYTEM DEMONSTARTOR: DESIGN AND ANALYSIS OF A MORPHING TRAILING EDGE DEMONSTRATOR USING HYPERELASTIC ADHESIVE

Jan Tikalsky
Institute of Lightweight Systems, German Aerospace Center (DLR)
Braunschweig, Germany

ABSTRACT

The biggest challenge of our time is the transition of aviation to climate neutrality and the move away from fossil fuels. Alternative fuels and energy storage systems go hand in hand with lower energy densities. This directly leads to higher fuel or system masses for the same range. The quotient of payload to required energy is dropping.

As a result, aerodynamic efficiency is the focus of future aircraft designs. One way of achieving this goal is to use morphing trailing edges that improve L/D, especially in off-design conditions.

However, the deformation of a morphing trailing edge changes the circumferential length of the airfoil section. This problem was often solved by slitting the pressure side of the wing, which cause a gap on a local section of the wing. Elastomers or sliding mechanisms are used to close this gap. Both lead to a deviation from the target shape and higher maintenance effort.

Pressurized solutions for camber morphing are in equilibrium between aerodynamic loads and internal forces. Therefore, additional measurement devices are required to determine the position of those systems.

In this work, a new approach is pursued by avoiding the slitting of the aerodynamically effective surfaces and using a compliant mechanism in the trailing edge. A conventional kinematic is introduced to drive the lower skin directly. Actuator moments are limited by use of non-linear transmission ratio of the kinematics.

The design and pre-dimensioning by analytical and finite element method (FEM) approach are presented. Based on this, a demonstrator was derived on the basis of the unmanned aerial system (UAS) PROTEUS from German Aerospace Center. PROTEUS has a span of 2950mm, a root chord of 595mm, an aspect ratio of 6 and V_d of 300 km/h. The demonstrator represents a 100 mm span morphing trailing edge section. To evaluate the prediction methods, drive forces and moments were calculated and compared using finite element method (FEM) as well as analytical methods.

In the comparison of both analysis methods, a very good correlation with a deviation of 0.5% was found for the actuator loads. The rod forces deviated from each other by approx. 5%.

Based on these results the prescribed demonstrator will be build and measurements on the kinematical loads and fatigue will be carried out to verify this concept for the implementation on PROTEUS.

Additionally, the wing demonstrator will be designed to determine internal loads performing spanwise differential deflections.

The UAS PROTEUS will then undergo flight tests determine L/D improvements using morphing trailing edges.

Keywords: Morphing, Wing, Trailing edge, Hyperelastic material, Compliant mechanism, HyTEM, Camber variation, Unmanned aerial system

1. INTRODUCTION

Trailing edge morphing wing technologies have been investigated for decades, but none of these technologies is implemented in industrial aircrafts. Camber morphing benefits of up to 20% on fighter type aircrafts, which was shown by [1–3] in late 1980’s / early 1990’s. Transonic passenger aircraft were investigated by [4, 5] showing a L/D potential by 2-3% using variable camber by using fowler flaps. Do Vale et al. [6] showed a further 2% L/D improvement potential by applying spanwise camber morphing.

Up to today just a few designs have been tested in flight [7]. The designs need to be load bearing and very flexible at the same time. That’s why these concepts often require high actuator loads and thus heavy actuators and kinematics. Thus, the system is getting more complex, which increases the manufacturing effort, the maintenance costs and the safety assessments.

HyTEM (Hyperelastic Trailing edge Morphing) is a new design principle, which is presented in this paper for implementing a camber variable morphing system. The skin concept will be introduced first, followed by a detailed examination of a complementary kinematic drive. Afterwards, the third part focus on the realization of a small-scale demonstrator. The last section compares the theoretical predictions with measurements of the demonstrator.

1.1. SKIN DESIGN CONCEPT

The biggest challenge for morphing designs is the wing skin, which undergoes changes in length due to the deformation. This results in large internal loads. Therefore, this problem is addressed first with a stiff and continuous skin. This enables a continuous transition of the profile surface into the deformable area without material change. The profile body remains continuous and step free.

As shown in Figure 1 , the concept envisages a closed profile body that is reinforced with a continuous skin (No. 15 and 16 in Figure 1). The connection of the trailing edge is realized with a compliant joint made of hyper elastic adhesive Sika-Pro3 (No. 17 in Figure 1).

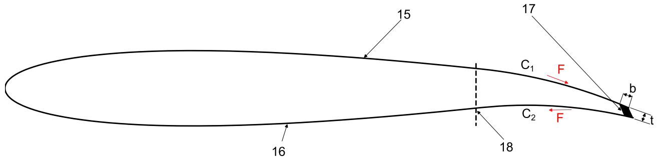

Figure 1: SKIN CONCEPT HYTEM [8]

This design of the outer geometry makes it possible to integrate variable shape trailing edges into conventional composite airfoil designs and at the same time remain free of steps and gaps. In addition, it is conceivable to have the shape variable area start at different profile depths on the upper and lower side via stiffness differences and thus vary the profile thickness in the area of the flap. No. 18 in Figure 1 shows the connection line between the deflection starting point on suction and pressure side. FIGURE 2 shows the principle that this line is tilted due to the flexible skin like entity 18 shows.

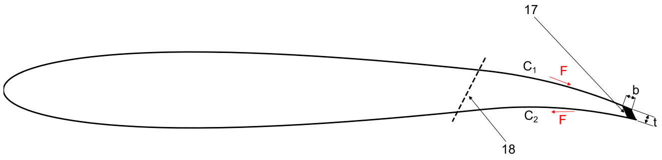

FIGURE 2: PROFILE THICKNESS VARIATION USING HYTEM [8]

The actuator requirements are reduced significantly in comparison to a rigid trailing edge connection. Literature [9] shows that the forces can be reduced to 0.01% - 0.1% with a compliant joint compared to a continuous rigid construction. Figure 3 shows the ratio $F_{Elastic}$ / F_{rigid} over the stiffness fraction ratio C_3 / C_1 where C_3 is the stiffness of the compliant joint and C_1 is the skin stiffness of a GFRP. b represents the width of the bonding. The grey area is the design space according to available materials and stiffness requirements.

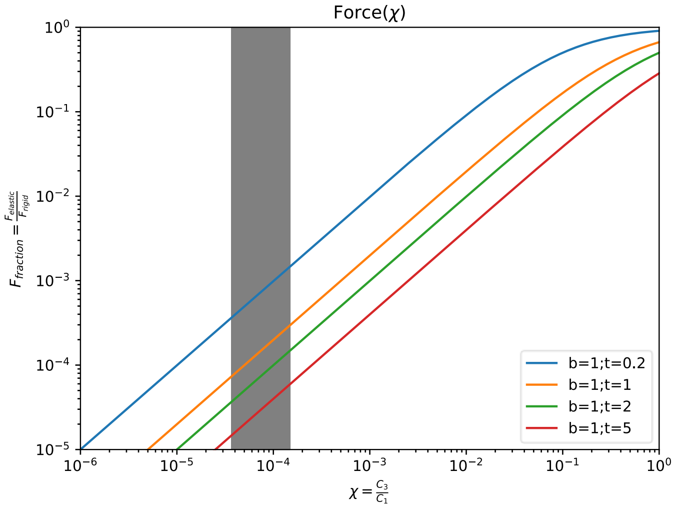

Figure 3: HYTEM POTENTIAL [9]

Due to the high elasticity, the cross section is torsional soft, so that the curvature of the profile can be used to generate differentiated deflections along the span. FIGURE 4 shows a sketch where the cross-sections at root and tip deflects downwards and the middle cross-section deflects upwards. Between those extremes there are cross-sections without any deflection.

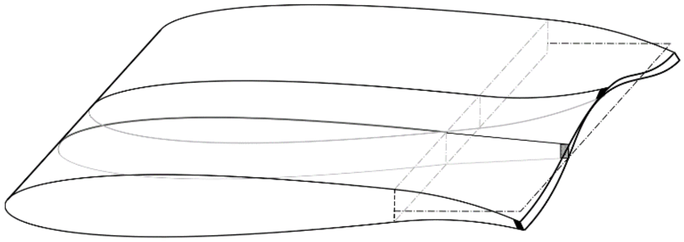

FIGURE 4: SPANWISE DIFFERENTIAL DEFLECTION

The spanwise differentiation can then be used to optimize the lift distribution depending on the flight operation point. This offers an aerodynamic potential to reduce the total drag. The design and the flight test on an UAS for such a spanwise differential morphing concept is one objective in DLR ongoing project MorphAIR [10].

1.2. ACTUATOR DESIGN CONCEPT

The particular challenge of this morphing concept is to find efficient and lightweight kinematics to introduce the necessary forces into the structure. Since the drive and the skin structure interact with each other, it is necessary to find a customized solution.

Many drive concepts are known. These tend to act near the end of the wing box and at the beginning of the flap. However, it is advantageous for the HyTEM concept if the deformation is initiated near the trailing edge.

Ideally, either a pure vertical force would be introduced at the end of the trailing edge, which is not feasible, or a horizontal displacement of one profile skin relative to the other would be generated.

Therefore, the approach of horizontal displacement of the lower skin is pursued. The loads transferred by the kinematics should met the actuator characteristic as precisely as possible minimize masses of the actuator.

In FIGURE 5, the deformation energy is applied by rotation of the actuator and transferred as longitudinal movement by a pushrod (1) close to the trailing edge of the airfoil (2). Considering force equilibrium, a and production of compression forces on the pressure side of the airfoil (3) results. Therefore, the compressive stresses in the composite skin on the pressure side decrease and the buckling safety is increased. That’s why the bending stiffness around the span axis can be reduced and a more flexible design can be selected for the wing shells. This leads to a load and weight reduction in two steps. On the one hand, the load bearing skins become lighter and on the other hand the actuator has to apply less deformation energy due to lower stiffness of the skins and can be smaller and lighter.

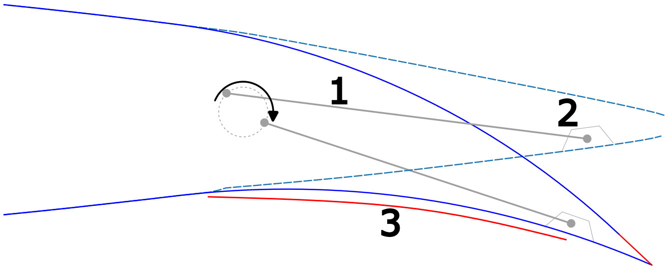

FIGURE 5: KINEMATIC SCHEME OF THE TRAILING EDGE WITH DEFORMED AND UNDEFORMED SKIN

Literature [9] shows that the deformation energy increases proportionally with the vertical displacement of the trailing edge tip. As a result, a servo would have to be designed for the maximum load and has to compromise speed for small deflections. Large deflections are expected to be used to change wing configuration, this adoption is done slowly. In contrast the operational speed of control surfaces as Ailerons is higher (in a range of 1-10 Hz [11]) but Amplitudes are smaller. Both requirements need to be met and this leads inevitably to very large servos.

For this reason, a non-linear kinematic system is proposed in Literature [12], which has a small transmission ratio for large degrees of deformation and large transmission ratios for small deformations. This is achieved here with the combination of an excentre with the pushrod (1) and a pivoted load introduction bracket (2).

2. ANALYTIC DESCRIPTION OF KINEMATIC

Before the kinematics can be designed, the maximum required deflection must be defined. In addition, the improved aerodynamic quality depends on the desired service life of the hyperelastic bonding. Frequent large deflections lead to short service life.

2.1. SERVICE LIFE TO DEFLECTION RELATION

Due to the viscoelastic material behavior of the adhesive, there are particular challenges in predicting the fatigue strength of hyperelastic adhesives. Literature [13] carried out tests on new and aged polyurethane based (PUR) and Silane Modified Compounds (SMC) adhesive samples. One temperature condition with a specific humidity condition was defined before design parameters were derived.

With the fatigue strength equation according to Woehler equation (1) a permissible shear stress amplitude τ_a can be calculated for a desired number of load cycles n with known k_w(Material dependent degradation value) and $\log \tau_{a,0}$ (shear stress amplitude cut off) [13].

$$\log \tau_a = \log \tau_{a,0} - \frac{1}{k_w} \log n \tag{1}$$

The allowable shear stress amplitude can be then derived by equation (2)

$$\tau_a = 10^{\log \tau_{a,0} - \frac{1}{k_w} \log n} \tag{2}$$

For reasons of harmonization, equations (3) and (4) are taken from Literature [13]. Where G is the shear modulus, τ_a the shear stress amplitude, T_n the undeformed thickness of the bonding and x is the shear displacement.

$$\hat{\Upsilon} = \frac{\tau_a}{G} \tag{3}$$

$$\hat{\Upsilon} = \frac{x}{T_n} \tag{4}$$

After transforming equations (2)-(4) , the permissible shear displacement can be specified as a function of the desired number of load cycles n as follows:

$$x(n) = \frac{\tau_a \cdot T_n}{G} = \frac{T_n \cdot 10^{\log \tau_{a,0} - \frac{1}{k_w} \log n}}{G} \tag{5}$$

Single lap shear tests from [9] are used to determine $\tau_{a,0}$. For Sika Pro-3, an average maximum stress of 0.952 N/mm² and a shear modulus G above the normalized displacement of 0.257 N/mm² were determined. k_w is taken from Table 1 and set at 5.76.

Table 1: Characteristic values for Aged PUR Adhesive for Woehler curves according to [13]

Characteristic values	Single lap shear
k_w	5.76

$\log \tau_{a,0}$	0.76
n	0.07

The trailing edge offset results from the geometric boundary conditions according to the following equation where a is half of the (rear) spar thickness and δ the trailing edge deflection angle from literature [9]:

$$x = 2 \cdot \mathrm{a} \cdot \tan(\delta) \tag{6}$$

This results in the following relationship for the possible deflection angle of the HyTEM system as a function of the desired number of load cycles.

$$\delta(\mathrm{n}, \mathrm{a}) = \mathrm{atan}\left(\frac{T_n \cdot 10^{\log \tau_{a,0} - \frac{1}{k_w} \log n}}{2 \cdot \mathrm{a} \cdot \mathrm{G}}\right) \tag{7}$$

2.2. UPPER PUSHROD PIVOT POINT DISPLACEMENT DETERMINATION

For simplification, it is assumed that the actuator acts linearly in x-direction, which assumes that the kinematics can be simplified to rigid body motions as FIGURE 6 shows. Driven by the movement of the upper pivot point from X_1 to X_2.

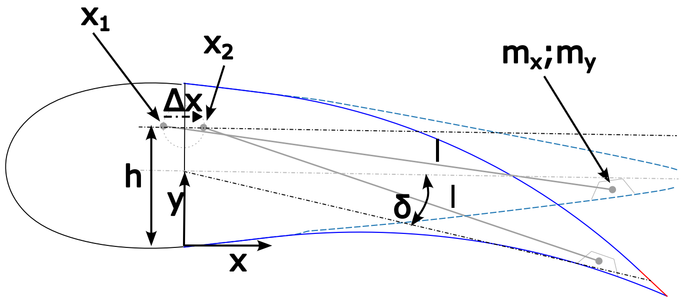

FIGURE 6: KINEMATIC MOVEMENT AND SKIN DEFORMATION STARTING AT THE (REAR) SPAR

First, equation (8) is used to calculate the relative x position dx_1 to the bracket connection point. Before the actual connection position to the actuator is shown in equation (9).

$$dx_1 = \sqrt{l^2 - (h - m_y)^2} \tag{8}$$

$$x_1 = m_x - dx_1 \tag{9}$$

To determine the support position, the equations in the deformed position (10) and (11) are given.

$$dx_2 = \sqrt{l^2 - (h - (m_y \cdot \cos(\delta) - m_x \cdot \sin(\delta))^2} \tag{10}$$

$$x_2 = \sqrt{m_y^2 + {m_x}^2} \cdot \cos(\delta) - \left(\tan^{-1}\left(\frac{m_y}{m_x}\right)\right) \tag{11}$$

Equation (12) describes the displacement of the actuator connection point in x direction.

$$\Delta x = x_2 - x_1 \tag{12}$$

2.3. TRANSMISSION RATIO DETERMINATION

The loads on the pushrod are made up of various components. On the one hand, there are the forces from the shear deformation (equation (13)), where l_y is the width and b is the span of the bonding.

$$F_\tau = G \cdot \hat{\Upsilon} \cdot l_y \cdot b \tag{13}$$

On the other hand, there is the elongation of the adhesive in the skin direction (equation (14)), where E describes the Young's modulus and ε the strain.

$$F_\sigma = E \cdot \varepsilon \cdot l_y \cdot b \cdot \cos\left(\frac{\pi}{2} - \arctan\left(\hat{\Upsilon}\right)\right) \tag{14}$$

Since the angle between the pushrod and these loads is small, the cosine can be simplified to be 1. The rod load results in equation (15) due to the bonding deformation.

$$F = F_\tau + F_\sigma \tag{15}$$

The forces due to the profile skin deformation are determined using the Bernoulli-Euler beam theory [14]. Since the deformation u_z is specified and skin Stiffnesses and geometry is known. This is converted according to the virtual force F_z placed at the end of the Trailing edge see Figure 7.

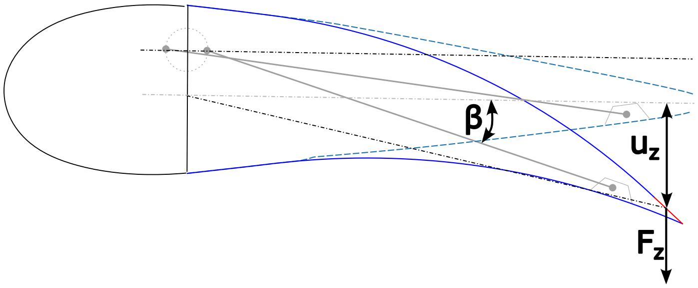

Figure 7: LOADS ON THE ADHESIVE IN DEFORMED SHAPE OF THE TRAILING EDGE

Furthermore, it is assumed that both airfoil skins have the same stiffness and carry the same load.

$$F_z = \frac{u_z \cdot EI}{{l_y}^3} \tag{16}$$

The vertical force must be balanced with the rod force acting at a flat angle. Here, β is the angle between horizontal line and the pushrod. This additional force results in equation (19)

$$F_{bending} = \frac{F_z}{\sin\beta} \tag{17}$$

Equations (13) to (15) show a proportional relationship between adhesive layer deformation and pushrod force. As discussed in chapter 1.2, the maximum servo torque is reduced via an excentre. FIGURE 8 shows a sketch of the trailing edge movement as a kinematic chain. The vertical displacement to pushrod length ratio is small (~0.1), the vertical motion is neglected resulting in a simplified kinematic model.

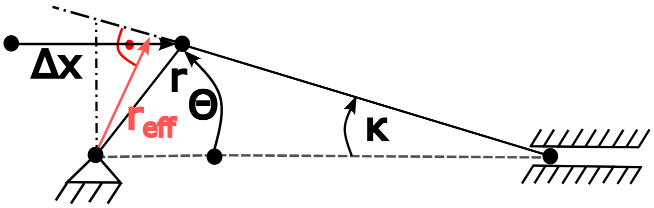

FIGURE 8: SIMPLIFIED KINEMATIC DESIGN IN A 2D DESIGN

Assuming that the excentric axis is parallel to the wing axis and perpendicular to the rod plane, the servo angle results in

$$\theta = \arccos\left(\frac{\Delta x}{2 \cdot r}\right); 0 \leq \Delta x \leq 2r \tag{18}$$

The maximum pushrod angle κ described by

$$\kappa = \arctan\left(\frac{r}{l}\right) \tag{19}$$

The quotient of r/l is very small so that κ is is simplified to be zero. The effective radius r_{eff} is determined to be:

$$r_{eff} = r \cdot \sin\theta \tag{20}$$

Due to the reduction of r_{eff}, the torque for large θ becomes small. This results in small torques at maximum flap deflections.

2.4. ADHESIVE MATERIAL PROPERTIES

The kinematic movement in FIGURE 6 shows a clear shear displacement of the adhesive, which is indicated with the red line at the trailing edge. Therefore, the material properties of the adhesive are determined by Single Lap Shear (SLS) test. The results from these tests can be read up in Literature [9]. The test configuration was simulated using Finite Element Method (FEM) as well as analytically according to equations (13) to (15).

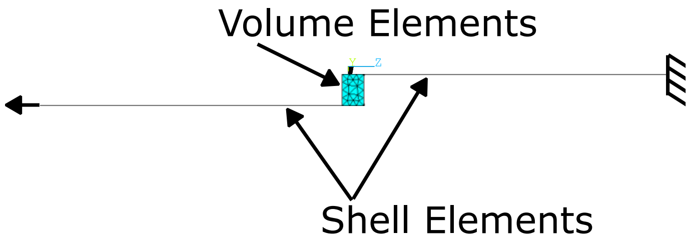

FIGURE 9: FEM MODEL (ANSYS® CLASSIC) OF THE SINGLE LAP SHEAR TEST IN SIDE VIEW

FIGURE 9 shows the model. On the right-hand side the model is fixed in all degrees of freedom, on the left side a displacement of 15mm is introduced. The laps are modeled as shell elements and the adhesive as volume elements. The geometry corresponds to the geometry of the test specimens from Literature [9].

The material properties were determined inverse by varying the Young's and shear moduli in such a way that they reflect the behavior of the tensile forces of the tested specimens. With initial shear modulus of 0.3084 [N/mm²] and material incompressibility parameter of 0.3084 [N/mm²], the curves shown in FIGURE 10 were obtained. The normalized shear $\hat{\Upsilon}$ is the quotient of shear displacement to bonding thickness.

The test results are shown with solid lines. A regression straight through the origin and the increase of 0.257 N/mm² shows a good prediction of linear material behavior with a correlation factor R^2 of 0.932 within the required dimensionless shear strain. This factor can be used for preliminary design calculations for moderate deformations. Nevertheless, the stiffness linear regression cannot be used for more detailed FE calculations. Due to high deformations, the loading condition changes from a pure shear to a tension-dominated load.

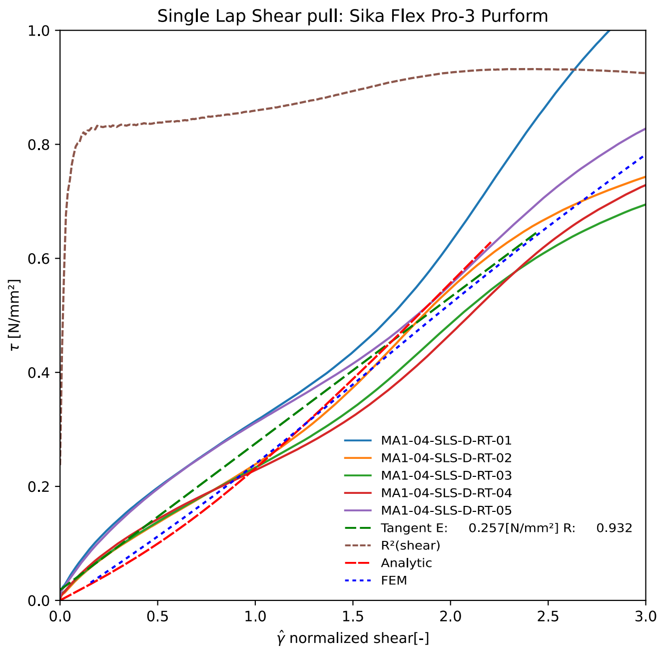

FIGURE 10: SLS TESTS OF SIKAPRO-3 COMPARED TO ANALYTICAL AND FEM RESULTS

It is noticeable that the calculated curves in small deformation ranges $\widehat{\Upsilon} < 1$ predict a lower stress than they were actually measured. For deformations $1 < \widehat{\Upsilon} < 2$, the calculations match the average of the measurements well.

It should be noted that the Mullins effect is not considered. Therefore, the calculated values reflect the loads for the first deformation of the adhesive. Subsequent deflections require a significantly lower force as the Young's modulus is dropping. This simplification leads to a reserve and thus to a conservative kinematic design. This reserve can be used for low environmental temperatures, for example.

3. DEMONSTARTOR DESIGN

The presented methods are used to design a demonstrator with an airfoil span of 100 mm. The test results of this demonstrator are analyzed compared with the values from section 2.

3.1. SELECTION OF A REPRESENTATIVE WING SECTION

HyTEM is to be used on DLR Unmanned Aerials System (UAS) PROTEUS with in the MorphAIR project. The wing of this UAS is the baseline for the cross- section selection for the demonstrator. FIGURE 11 shows the wing plan form shape and the position of the selected section with a dashed line.

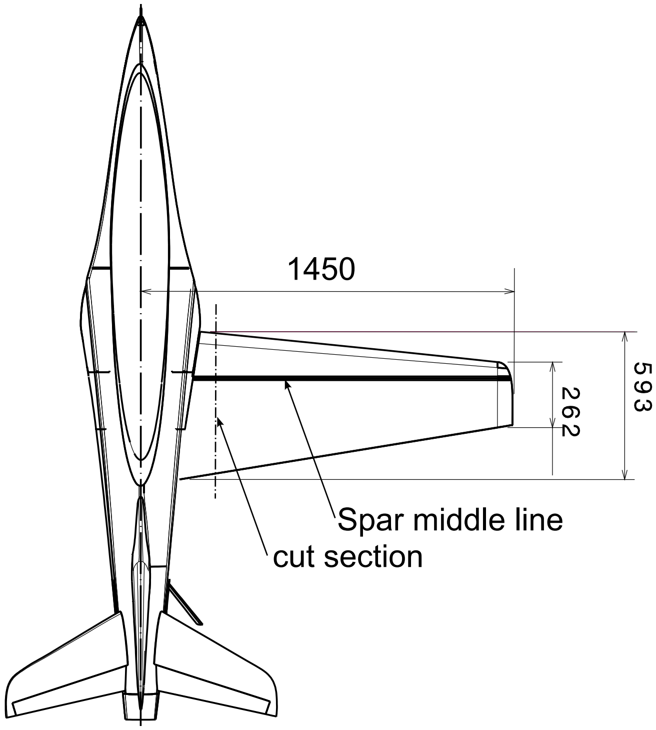

FIGURE 11: CAD MODEL OF THE WING PLANFORM WITH THE SELECTED SECTION CUT DASHED DIMENSIONS IN MILLIMETERS

At this section, the spar thickness is large and the length of the shape variable flap is proportionally long. In relation to equation (6), this represents an unfavorable and therefore conservative combination of spar thickness and flap chord length. In order to simplify the production of the demonstrator, the spar geometry is a metallic C-shaped structure, as it can be seen in FIGURE 12. In addition, the rearward profile curvature was abstracted with plates. FIGURE 12 shows the plates compared to the profile curvature, which is shown as faded line. The installation space for the bracket near the trailing edge is thus considerably reduced. This is also on the conservative side for future realization on the real wing profile.

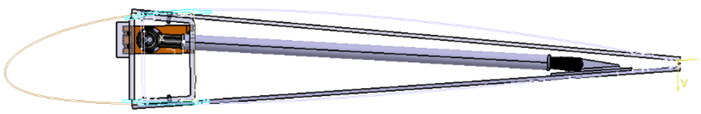

FIGURE 12: CROSS SECTION VIEW OF THE DEMONSTRATOR COMPARED TO THE ORGINAL WING PROFILE

It can be assumed that the spar is often not parallel to the trailing edge. Therefore, the actuator is rotated by 10° relative to the trailing edge (FIGURE 13) to deliver a more representative kinematic.

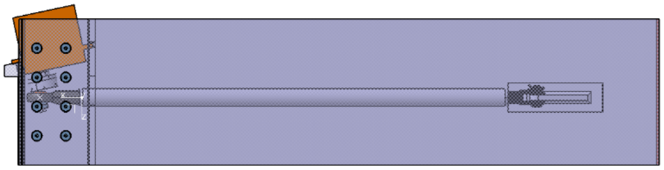

FIGURE 13: DEMONSTRATOR TOP VIEW WITH NON-PARALLEL ACTUATOR POSITIONING

The actual geometry with the dimensions in millimeter required for the calculation are shown in FIGURE 14.

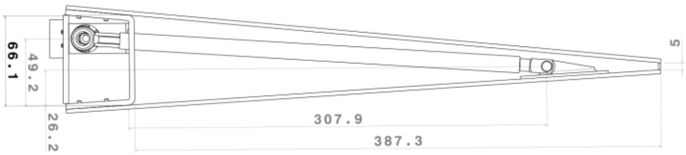

FIGURE 14. DEMONSTRATOR GEOMETRY

3.2. HIGH-FIDELITY MODEL

The model for the finite element method is shown in FIGURE 15. The model replaces the excentre and the pushrod with rigid rod elements. Both rods are connected via a universal joint. Node 2B of strut 2 is fixed in position and rotate only around the servo axis. Strut 1 is in turn rotatable to the bracket.

This means that the desired rotation can be specified as a boundary condition at node 2B. The model is fixed at the ends as shown in FIGURE 15.

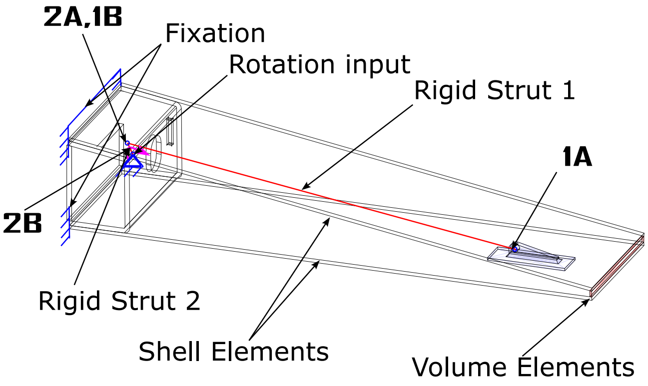

FIGURE 15: SIMPLIFIED FEM MODEL WITH RIGID EXCENTRE (STRUT 2) AND PUSH ROD (STRUT 1)

Layered shell elements are used for the skins. While the rest of the model is represented by solid elements as FIGURE 16 shows. The excentre rotated in line with the pushrod. The shell layup is a sandwich with [0° interglas 92110; 90° interglas 92110; 2mm R51 foam; 90° interglas 92110; 0° interglas 92110].

Properties of one interglas 92110 layer in hand lay-up lamination (E1=E2: 22500 N/mm²; υ: 0.35; thickness: 0.22mm) and R51 foam (E: 45 N/mm² υ: 0.32).

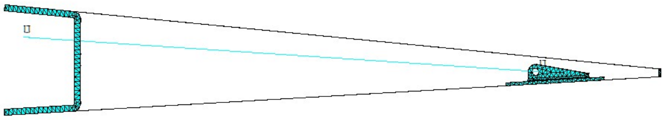

FIGURE 16: SIDE VIEW OF THE FEM MODEL WITH ELEMENTS FOR SOLID BODIES

Due to the stiffness dependence on the deformed geometry the solution of the model must be geometrically non-linear. Very high strains are expected in the range of 100%-200% in the bonding, which deteriorates the elements aspect ratio with increasing displacements. Additionally, the stiffness of adhesive elements is very low compared to the rest of the model. As a result, convergence problems are expected as the stiffness matrix becomes almost singular. This problem is solved by remeshing the elements with unfavorable aspect ratios during solution. The remeshing takes place between the time steps of the non-linear calculation and uses the already deformed geometry. So, the convergence is approved significantly.

4. RESULTS AND DISCUSSION

The service life curves of the HyTEM concept are discussed first, before the calculated forces and moments of the kinematics are compared to the analytical results.

4.1. SERVICE LIFE ESTIMATION

FIGURE 17 shows the relationship between the expected number of load cycles and the displacement of the kinematic point as shown in FIGURE 6. PUR and SMA adhesives are subject to soften du to Mullin’s effect. FIGURE 17 considers the initial state of the material neglecting any softening effect.

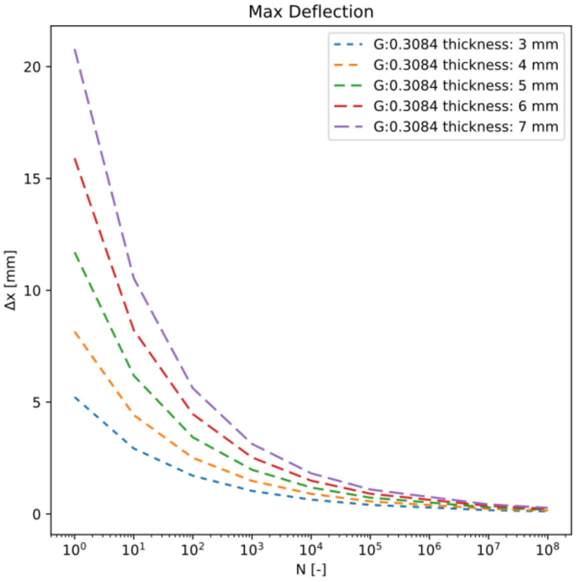

FIGURE 17: SERVICE LIFE CURVES FOR ACTUATOR TRANSLATION WITH INITIAL SHEAR MODULUS

FIGURE 18 shows the service life curves over the deflection angle of the trailing edge. In both diagrams it can be seen that the curves are strongly decreasing. An adhesive layer thickness of 5 mm was selected for the demonstrator shown here. The maximum service life of the demonstrator is set at 10^3 load cycles in order to limit the test duration until failure, but being able to check the consistency of this model. This means that a δ of 5° or Δx of 2,5mm deflections would be possible with this number of load cycles. It has to be remarked that the measurements of the underlying coefficients from [13] is based on a constant stress amplitude. This is not the application of HyTEM and leads to pessimistic lifecycle forecasts.

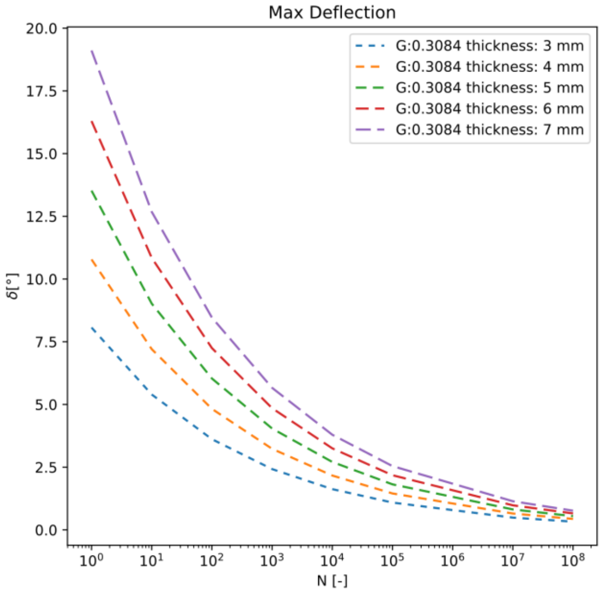

FIGURE 18: SERVICE LIFE CURVES FOR FLAP DEFLECTION

A constant displacement is provided in this application. Due to the Mullins effect, the stiffness decreases while repeating deformations. The occurring bonding stress becomes smaller. FIGURE 19 shows an oscillating SLS with constant displacement amplitude. The first (orange) deformation generates significantly higher stresses than the subsequent ones (blue).

The Young's modulus for the deformations after the first deformation cycle can be approximated with a regression line. $\bar{G}$ as determined to be 0.145 N/mm^2 and a correlation factor of 0.906.

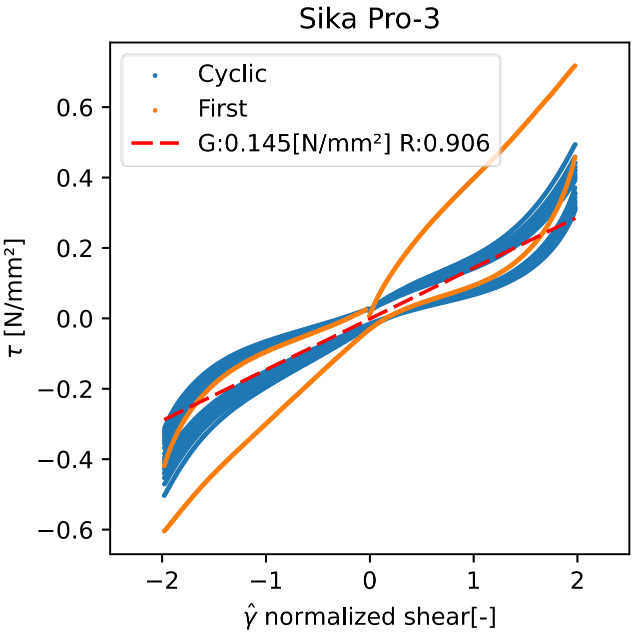

FIGURE 19: OSCILLATING SLS TEST OF SIKA PRO-3

FIGURE 20 shows the maximum possible deflection over the number of cycles for the same geometry and adhesive dimensions with different stiffnesses in relation to the Mullins effect. This results in a significantly higher deflection for the same number of load cycles.

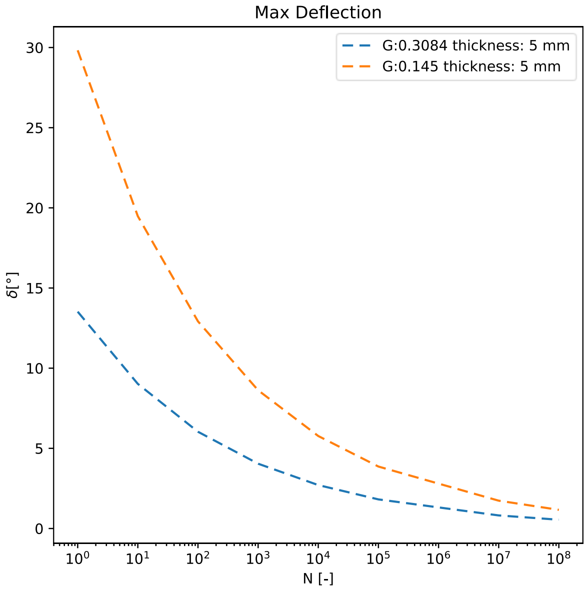

FIGURE 20: SERVICE LIFE AT DIFFERENT SHEAR MODULI

A maximum flap deflection angle of 10° was selected for the demonstrator in relation to required flap deflection at UAS PROTEUS. This results in an eccentricity of 4 mm and it allows a limited test duration. In this case, a number of cycles between 6 (initial shear modulus) and 470 (softened shear modulus) is expected. Additionally, the reduced shear modulus leads to a reserve in the kinematics, which can be used for lower temperatures when adhesive stiffness increases.

4.2. COMPARISSON OF KINEMATIC MODELS

The deformed geometry was simplified for the derivation of the analytical solution. Therefore, the effective radius between the servo axis of rotation and the pushrod is plotted in FIGURE 21. There is a deviation in the end positions of both solutions. The effective radius of the FEM solution is 0.25 and 0.5 mm larger in the end positions than that of the analytical solution. The end-positions do not influence the flap deflection and servo moment as r_{eff} is very small. As soon as the end points are left, both radii approach each other and are largely coincident. This shows that the simplifications were permissible and represent the system sufficiently accurately from a geometric perspective.

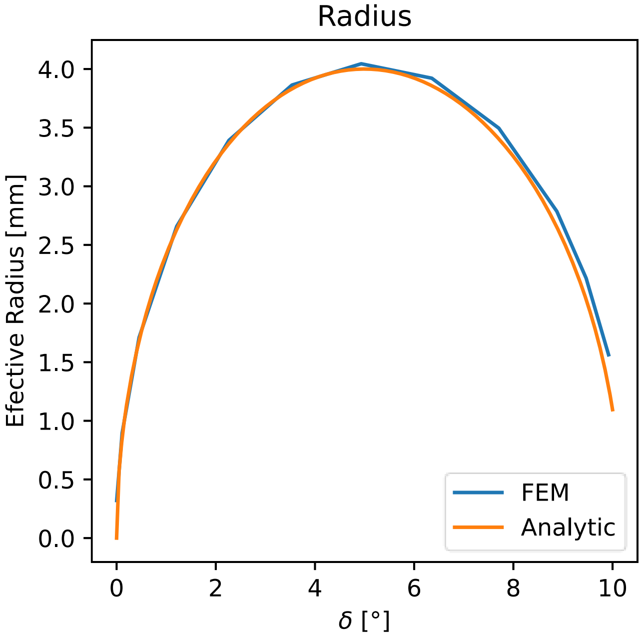

FIGURE 21: COMPARISON EFFECTIVE RADIUS

4.3. KINEMATIC LOADS

The loads were calculated with the initial values (0.3084 N/mm²) of the adhesive stiffness, which represents the conservative case for the design.

The loads of the pushrod are first compared between the analytical and the FEM method.

FIGURE 22 shows the progression of the curves. The analytical solution without consideration of the profile skin bending and the FEM solution shows a similar characteristic curve, but deviate from each other by approx. 31%. The analytical solution with consideration of the airfoil skin bending shows a more strongly increasing curve and agrees better with the results of the FEM.

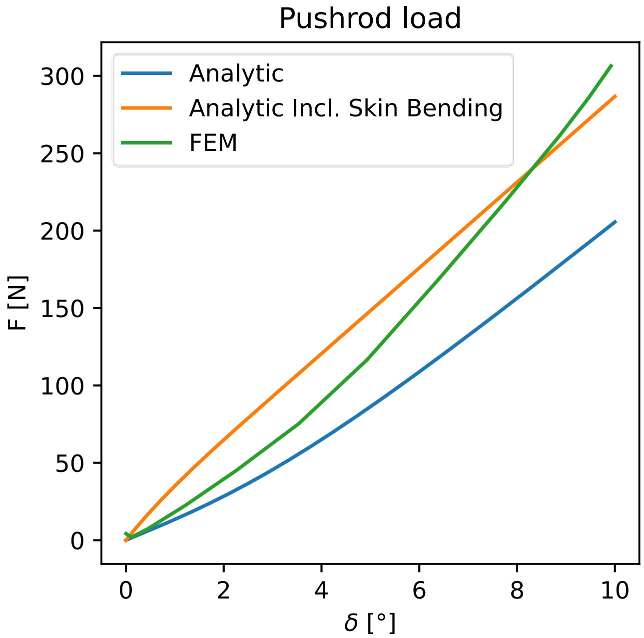

FIGURE 22: PUSHROD LOADS

Therefore, the structural deformation must be considered when designing the kinematics. A more precise consideration of the deformation energy of the wing skins would further increase the accuracy. However, the goal is a simple prediction method and the deviation is acceptable in this case. If the use of an excentre is neglected within a design, the maximum force from the pushrod would have to be used for dimensioning. As it can be seen, the force curve in FIGURE 22 increases proportionally with the deflection of the flap. The actuator must represent a compromise between movement speed and force. This potentially leads to heavy actuators, when the flap has multiple tasks like acting as high lift system with large deflection and acting as load alleviation system with high frequent deflections.

FIGURE 23 shows the servo torque curves using an excentre. All curves show a similar progression. First the curves rise up to an angle δ of approx. 6.4° and then reach a maximum between 7.4° and 8°. After that, the moments drop rapidly.

The analytical solution without the skin bending shows a large deviation from the FEM solution. In contrast, the maxima of the analytical solution with profile skin bending and FEM agree well. The difference is 0.5 % in the maximum moment and 2.8 % in the angular position, which is considered to be sufficiently accurate for a prediction.

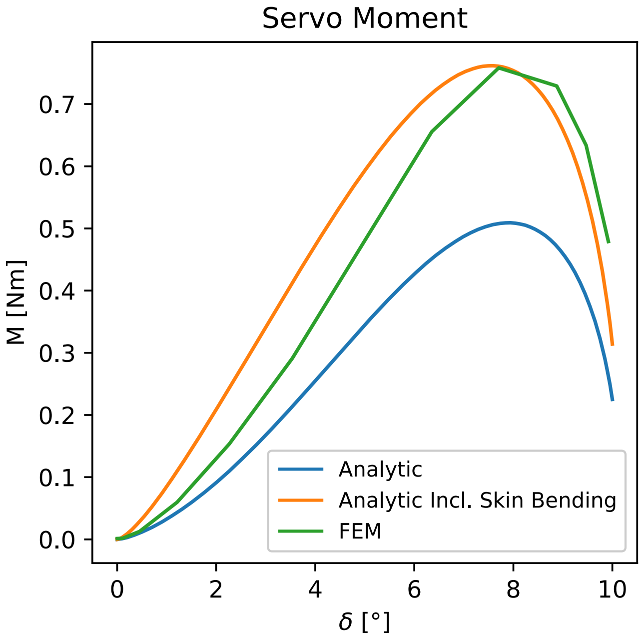

FIGURE 23: ACTUATOR MOMENTS

5. CONCLUSION AND OUTLOOCK

The presented results suggest that the analytical method incorporating profile skin bending is suitable for the preliminary design of a HyTEM system. The deviation of the moments of less than 2.8% enables future optimizations. The presented procedure will be validated by carrying out a number of tests including static deformation as well as cyclical deformation for fatigue evaluation. Additionally, deformation measurements are planned to be compared to the FEM method. This analytical method needs to be extended to predict kinematic loads inside the wing, which is deflecting differentially along the span. This will be used to design and evaluate the wing demonstrator for the UAS PROTEUS. PROTEUS will finally undergo flight testing for overall aircraft performance and internal structural loads improvement.

6. REFERENCES

[1] AFWAL-TR-88-3082, ed., *AFTI/F-111 Mission Adaptive Wing Briefing to industry. Final Report*, 1988.

[2] John W. Smith, wilton P. Lock, Gordon A. Payne, “Variable-Camber Systemsintegration and Operational Performance of the AFTI/F-111 Mission Adaptive Wing: NASA Technical Memorandum 4370,” NASA Technical Memorandum 4370, 1992.

[3] Sheryll Goecke Powers, Lannie D. Webb, Edward L. Friend, William a. Lokos, “Flight Tests Results From a Supercritical Mission Adaptive Wing With Smoth Variable camber: NASA Technical Memorandum 4415,” *NASa Technical Memorandum, No.* 4415, 1992.

[4] Greff, “Stand der Aerodynamik-Arbeiten zum FFE-Vorhaben "Funktion des Intelligenten Flügels" (Status of aerodynamic works for FFE "Function Of Intelligent Wings"),” 21 Jan. 1991.

[5] “SIP-Projekt: Flügel Variabler Wölbung (Wing Of Variable Chamber),” TK 62/099/92, 10.1992.

[6] do Vale, J. L., Afonso, F., Lau, F., and Suleman, A., “Span Morphing Concept: An Overview,” *Morphing Wing Technologies,* Elsevier, 2018, pp. 125–144.

[7] Barbarino, S., Bilgen, O., Ajaj, R. M., Friswell, M. I., and Inman, D. J., “A Review of Morphing Aircraft,” *Journal of Intelligent Material Systems and Structures*; Vol. 22, No. 9, 2011, pp. 823–877. doi: 10.1177/1045389X11414084.

[8] Jan Tikalsky, *patent application: elastische Hinterkantenverklebung(Elastic Trailing edge Bonding), 10 2023 117 337.5*, 30.06.2023.

[9] Jan Tikalsky, “Morphing Compliant Trailingedge Skin Concept,” [online], https://www.researchsquare.com/article/rs-3996937/v1, [retrieved 12.03.24].

[10] M.Radestock, *DLR UAS TEST PLATFORM FOR MORPHING WINGS*, Austin (TX), USA, September 2023.

[11] Jayanath N. Kuduva, Allen J. Lockyer, Kari Appa, “Adaptive Aircraft Wing,” *Smart Structures and Materials*, 1996.

[12] Jan Tikalsky, *patent application: Trailing edge drive, 2024020912232000DE*, 24.07.2024.

[13] DVS Forschungsverenigung (Publisher), “Nachweis Beanspruchung hyperelastische Klebverbindungen unter betriebrelevanten Bedingungen II: Proof of stress on hyperelastic bonded joints under operationally relevant conditions II,” *549,* DVS-Nr.: 08.3117, 2022.

[14] H.Balke, *Einführung in die Technische Mechanik. Introduction to engineering mechanics*, Springer Nature, 2010.